Constructing Molecular Junctions with High-Spin Metal Sites in POMOFs to Trigger Heteropoly Blue States for Photocatalytic H_2 Production

*Weize Sun[‡a], Bo Zhao[‡b], Carlos J. Gómez-Garcíac, Haijun Pang[*a], Zhongling Lang[*b], Huiyuan Ma[a], Xinming Wang[a], Guixin Yang[a], Chi-Ming Au[d] and Wing-Yiu Yu[*d]*

[a]*School of Materials Science and Chemical Engineering, Harbin University of Science and Technology, Harbin, 150040, P. R. China. Email: panghj116@163.com (HJ Pang)*

[b]*Key Laboratory of Polyoxometalate and Reticular Material Chemistry of Ministry of Education, Faculty of Chemistry, Northeast Normal University, Changchun 130024, China. Email: langzl554@nenu.edu.cn (ZL Lang)*

[c]*Departamento de Química Inorgánica. Universidad de Valencia. C/Dr. Moliner 50. 46100 Burjasot, Spain.*

[d]*State Key Laboratory of Chemical Biology and Drug Discovery and Department of Applied Biology and Chemical Technology, The Hong Kong Polytechnic University, Hung Hom, Kowloon, Hong Kong. Email: wing-yiu.yu@polyu.edu.hk (WY Yu)*

ABSTRACT: The spin state of metal atoms may play a key role on the photocatalytic hydrogen evolution reaction (HER) of polyoxometalate (POM)-based catalysts. Herein, we construct two POM-based metal-organic frameworks (POMOFs) with molecular junction structures by integrating metal-organic framework structure including high spin-state active Co or Ni sites with $[GeW_{12}O_{40}]^{4-}$ (GeW_{12}) POM. These structures have a fast electron transfer channel, in which the electronic structures of the high spin metal centers may determine whether the POM can produce reduced POM (heteropolyblue, HPB) leading to enhanced HER activity. Upon photoexcitation, the Co^{II} high-spin state has a vacant in the t_{2g} orbital, that transfers electrons through π-orbitals, enhancing the electron transfer rate and promoting the generation of HPB. Thus, Co_6-GeW_{12} POMOF forms HPB species during the photocatalytic process and has a photocatalytic HER activity as high as 13.7 mmol g^{-1} h^{-1}. This value is the highest one obtained for any photocatalysts with POM as photosensitizer.

KEYWORDS: polyoxometalate, molecular junction, high spin-state, heteropolyblue, photocatalytic HER

INTRODUCTION

Hydrogen, as a sustainable and efficient source, has become a key area of research in the last decade.[1] Photocatalytic decomposition of water is one of the possible ways to obtain hydrogen, in which the photocatalyst is the key factor to determine the efficiency of hydrogen production. Noble metals have good photocatalytic activity and are commonly used to participate in photocatalytic reactions, but their high price greatly increases the cost of application.[2-4] Hence, considerable effort has been dedicated to the development of efficient non-noble photocatalysts such as metal oxide semiconductors, metal sulphides and metal-organic frameworks (MOFs).[5-8]

In metal complexes, the spin state of the metal center has a significant effect on the catalytic performance. The spin state can be mainly classified into two states: low and high spin (HS). The HS state is observed when the energy difference between the t_{2g} and e_g orbitals is low, whereas low spin is observed when this energy difference is high. In addition, during the HER process, H atom adsorption and O-H bond breaking are is strongly influenced by the electronic structures of the metal sites.[9] In groups 9 metals, especially Co, HS metallic centers can accelerate the light-induced charge separation, decrease the free energy of adsorbed H atoms and the activation barrier for the formation of H-H bonds.[10-13] Therefore, the synthesis of catalysts with HS Co as metal active centers is a feasible strategy to obtain efficient catalyst with for HER.

Polyoxometalates (POMs) are a class of nanoscale metal oxide clusters with numerous desirable properties, including structural stability, tunable size and anionic charge, catalytic ability, reversible redox activity and semiconductor-like properties. Therefore, they have a great potential for application in photocatalytic water splitting.[14-16] Nevertheless, POMs generally only absorb in the UV region because of their low LUMO energy level and big HOMO-LUMO energy gap.[17] Keggin-type polyoxometalates are able to form 24-electron super reduced state heteropoly blue species, which can absorb visible light and enhance the utilisation of light energy, thus achieving improved photocatalytic activity.[32,33] Therefore, Keggin-type polyoxometalate are ideal precursor materials for the synthesis of photocatalysts.

POM-based metal-organic frameworks (POMOFs), as crystalline porous materials, are formed by POMs and/or metal ions or clusters bridged with organic ligands with some unique advantages: i) high porosity and large surface area for photocatalytic hydrogen production, ii) MOFs also provide organic ligands with a regular porous structure that increases the stability of the overall structure. iii) well-defined metal coordination environments facilitate precise

mechanistic investigations, while the tunable composition of metallic active sites offers additional flexibility in catalytic design, iv) the incorporation of transition metal elements (such as Fe, Co, and Ni) within MOF structures can enhance the LUMO energy levels of POMOF photocatalysts through orbital coupling.[8,18-27]

Evermore, in addition to the above advantages, POMOFs with periodically ordered molecular structures are non-precious metal photocatalysts able to build intramolecular heterojunctions for rapid electron transfer.[28-31] In fact, heteropolyblues (HPBs, since reduced heteropoly POMs are generally deep blue) can be easily obtained by reduction of POM. HPBs show high absorption in the visible region (400-800 nm), enlarging the light absorption range of pure POM.[32-34] The reduction of HPBs in POMOFs may occur in two main ways: i) organic solvents provide electrons to the POM, resulting in the reduction of W^{6+}/Mo^{6+} to W^{5+}/Mo^{5+} and ii) the metal in the MOF can be excited by light to provide electrons to the POM, resulting in the reduction of W^{6+}/Mo^{6+} to W^{5+}/Mo^{5+}.[35-37]

In summary, POMOFs are promising candidates as non-noble photocatalysts for efficient hydrogen production. Albeit, the existence of the organic ligands may hinder the contact of the POM with the electron donor, inhibiting the reduction of the POMOF to the HPB state when undergoing the photocatalytic hydrogen production process and, therefore, reducing the photocatalytic activity.[38] In addition, the different arrangement of the metal electrons in the metal complexes orbitals will lead to different ligand field stabilization energies (LFSE) affecting, on one hand, the stability of the structure and, on the other hand, the electron transfer efficiency. Therefore, it is necessary to select suitable metal elements to construct POMOFs structures capable of forming HPB states. Ideal structures of POMOFs should: i) be able to form HPB states during the photocatalytic process to enhance the absorption of visible light, ii) build fast

electron transfer channels by molecular junctions to improve the transfer efficiency of the photogenerated electrons, iii) be constructed from non-precious metals and iv) be easily recycled.

In this work, we take advantage of the difference in the electronic configurations between Co and Ni to investigate their effect on the formation of reduced HPBs and consequently, on the catalytic HER activity of two closely related POMOFs. On the other side, we use the pzta ligand (5-(2-pyrazinyl)triazole) since it has a high capacity to connect metals centers to ensure the formation of POMOFs structures. (Figure S1). Based on these two points, we have prepared two POMOFs: $[Co^{II}_6(pzta)_6(H_2O)_4(OH)_2](GeW_{12}O_{40})$ (abbreviated as Co_6-GeW_{12}) and $[Ni^{II}_6(pzta)_6(H_2O)_4(OH)_2](GeW_{12}O_{40})$ (abbreviated as Ni_6-GeW_{12}) by hydrothermal methods (Scheme S1). These two crystalline compounds have the same structure and, therefore, allow to study the effect of two different transition metals on the photocatalytic HER activity of these POMOFs. The introduction of Co and Ni significantly increases the photocatalytic HER activity of these POMOFs compared to those of the parent polyoxometalates. We show that the transition metals can act as active sites to improve the electron transfer of the photogenerated electrons to the H^+. The Co-containing POMOF Co_6-GeW_{12} exhibits a better hydrogen evolution rate (up to 13.7 mmol g^{-1} h^{-1} with a Turnover Number (TON) of 349.8 and a Turnover Frequency (TOF) of 58.3 h^{-1}). The better performance of the cobalt POMOF compared to the Ni one can be explained by the differences in the electronic configurations (high-spin $t_{2g}^5e_g^2$ for Co^{II} and $t_{2g}^6e_g^2$ for Ni^{II}). The lower LFSE of Co^{II} in Co_6-GeW_{12} can be more easily overtaken, allowing, on one hand, a better contact between the sacrificial electron donor and the POM to form the HPB state. On the other hand, the electrons in the t_{2g}^5 orbitals can be transferred to the POM through W-O-Co π-bonds.

The synergistic outcome of these two facts leads to the formation of HPBs from Co_6-GeW_{12}. DFT calculations show that the photogenerated electrons produced by the reduced HPBs can be transferred back to Co^{II} via π-bonds, thus providing a high photocatalytic activity. Remarkably, Co_6-GeW_{12} is the photocatalyst for H_2 evolution with the highest catalytic activity among classical $(GeW_{12}O_{40})^{4-}$ and demonstrates superior photocatalytic performance compared to any POM-based photocatalysts.

METHODS

Synthesis of Co_6-GeW_{12}. $K_4(GeW_{12}O_{40})\cdot 7H_2O$, $CoCl_2\cdot 6H_2O$ (0.16 g), NH_4VO_3 (0.35 g) and pzta (0.45 g) were dissolved in 36 mL of deionized water and the pH was adjusted to 6.8 with 1 M HCl or NaOH solution. The resulting solution was stirred at room temperature for 2 h and was divided into three aliquots that were transferred to a 20 mL PTFE reactor and kept at 180 ºC for 72 h. The reactor was allowed to slowly cool in the oven down to 80 ºC to obtain brown-red rhombic crystals that were filtered, washed with water and air-dried to obtain Co_6-GeW_{12}.

Synthesis of Ni_6-GeW_{12}. Ni_6-GeW_{12} was synthesized as Co_6-GeW_{12} but adding $NiCl_2\cdot 6H_2O$ (0.16 g) instead of $CoCl_2\cdot 6H_2O$ and adjusting the pH of the solution to 6.6. The brown-green rhombic crystals so obtained were also filtered, washed with water and air-dried.

RESULTS AND DISCUSSION

Both compounds are isostructural and crystallize in the trigonal *R*3 space group.[39] The asymmetric unit consist of two Co (or Ni) atoms, two deprotonated $pzta^-$ ligands, two coordinated O atoms (O1W and O2W) and 1/3 $(GeW_{12}O_{40})^{4-}$ POM. Thus, the formula of compounds is $[M^{II}_6(pzta)_6(H_2O)_4(OH)_2](GeW_{12}O_{40})$ (M = Co or Ni). Note that although it is not possible to find the H atoms attached to the coordinated O1W and O2W atoms, the charge balance requires that two of the six oxygen atoms of the formula unit to be OH^- groups and water

molecules the other four.[40,41] The two independent M^{II} ions (M1 and M2) show slightly distorted octahedral coordination geometries of the type MN_4O_2 (Figure S5). In both centers the four N atoms correspond to a chelate and two monodentate pzta$^-$ ligands, whereas the two O atoms are a water molecule (or a hydroxide anion) and a terminal O atom of the $(GeW_{12}O_{40})^{4-}$ POM. The bond distances of Co-O, Co-N, Ni-N and Ni-O are all similar (Tables S3 and S4).

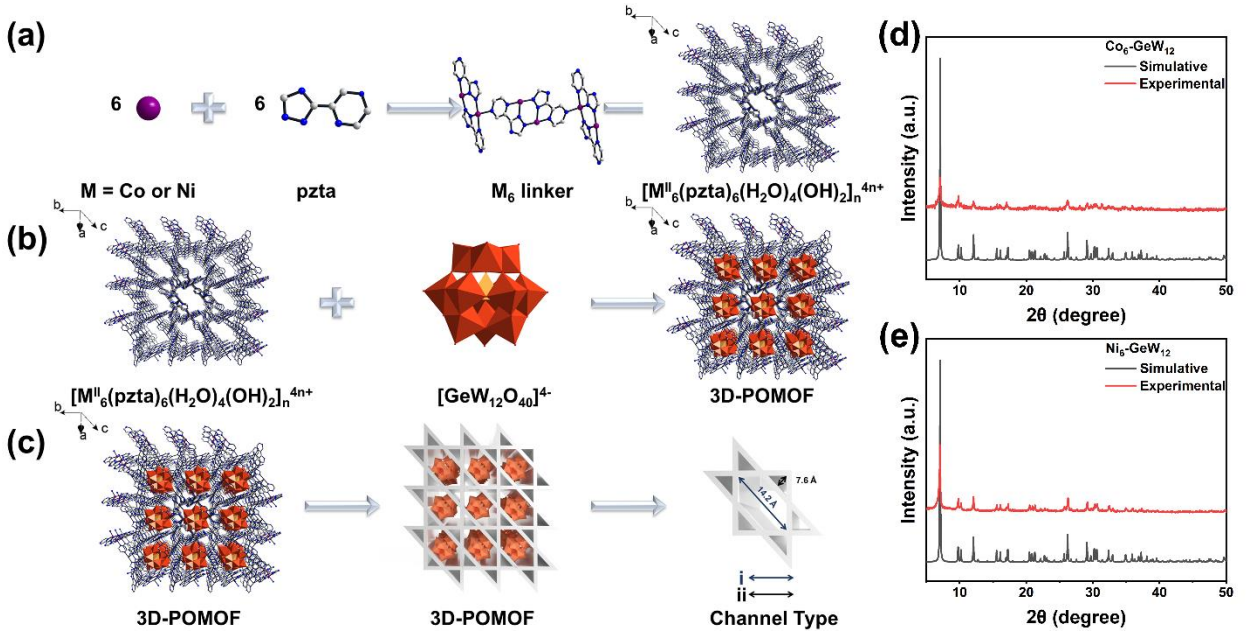

Figure 1. Schematic construction of the structure of M_6-GeW_{12} (M = Co or Ni): (a) $[M^{II}_6(pzta)_6(H_2O)_4(OH)_2]_n^{4n+}$; (b) 3D-POMOF and (c) channel types; Simulated and experimental X-ray powder patterns of (d) Co_6-GeW_{12} and (e) Ni_6-GeW_{12}.

The pzta$^-$ ligands connect the M^{II} ions to form the hexanuclear cationic entity $[M^{II}_6(pzta)_6(H_2O)_4(OH)_2]^{4+}$ (I) (Figure 1a). The M^{II}_6 units are further connected via M-N bonds to form a cationinc $[M^{II}_6(pzta)_6(H_2O)_4(OH)_2]_n^{4n+}$ with two types of channels (i and ii, Figure 1c). The bigger channels (i) are large enough to accommodate the $(GeW_{12}O_{40})^{4-}$ POMs that connect to the via the terminal O atoms of the POMs (O_t). These M-O_t bonds fix the POMs in the channels, increase the stability of the and create molecular junctions in the 3D-POMOF structure

(Figure 1b). Analysis of the porosity of the crystal using PLATON software yields an effective porosity of 253.0 $Å^3$ per unit cell, which is 4.3 % of the total cell volume of 5901.0 $Å^3$. This effective porosity corresponds to the smaller channel (ii, with a size of 7.6 Å, Figure 1c). This empty channel allows the easy diffusion of H_2O and H^+, favoring the formation of photoactive sites and increasing the efficiency of the photo-driven water separation reaction. The X-ray powder diffractogram of both compounds coincide with the simulated ones from the single crystal data, confirming the purity of the two compounds (Figures 1d and 1e).

The oxidation states of Co, Ni and W were verified through X-ray photoelectron spectroscopy (XPS). The Co^{II} 2p orbitals of Co_6-GeW_{12} show two distinct peaks at 780.62 and 796.52 eV, corresponding to the $2p_{3/2}$ and $2p_{1/2}$ energy levels. (Figure 2a). The peaks at 786.0 and 801.88 eV correspond to the satellite peaks of Co^{II}.[42-45] In addition, the spin-orbit splitting energy (ΔE_{2p}), increases with the amount of unpaired electrons of Co atom. In our case, ΔE_{2p} is 15.9 eV, very similar to the reported values for divalent HS Co^{II} ions. There is, additionally, a satellite characteristic peak which further the presence of HS Co^{II} ions.[13, 46] Therefore, the XPS spectrum indicates the presence of high-spin Co^{II} ions that present, in a octahedral coordination, a $t_{2g}^5e_g^2$ electron configuration, i.e., with one unpaired electron in the t_{2g} orbital and two unpaired electrons in the e_g orbitals. This electronic configuration facilitates the electron transfer through the π-bonds of the terminal O atoms, showing potential for excellent photocatalytic properties.

The peaks observed at 855.34 and 872.92 eV in the Ni_6-GeW_{12} compound can be assigned to the Ni^{II} $2p_{3/2}$ and Ni^{II} $2p_{1/2}$ orbitals, respectively. On the other hand, the presence of the additional peaks at 861.22 and 878.84 eV indicates the presence of satellite peaks associated with Ni^{II} (Figure 2c).[47] Ni^{II} in an octahedral environment has a $t_{2g}^6e_g^2$ electron configuration, with no unpaired electron in the t_{2g} orbital and two unpaired electrons in the e_g orbitals. Therefore, Ni^{II}

cannot transport electrons through the t_{2g} orbitals from the O atoms of the GeW_{12} clusters. In both compounds, the peaks of W $4f_{7/2}$ and W $4f_{5/2}$ appear at identical binding energies of 34.4 and 36.5 eV, respectively, indicating the presence of W^{VI} ions. Additionally, we observe satellite peaks at 40.2 eV in Co_6-GeW_{12} and 39.9 eV in Ni_6-GeW_{12}, corresponding to W^{VI} can be observed (Figures 2b and 2d).[36]

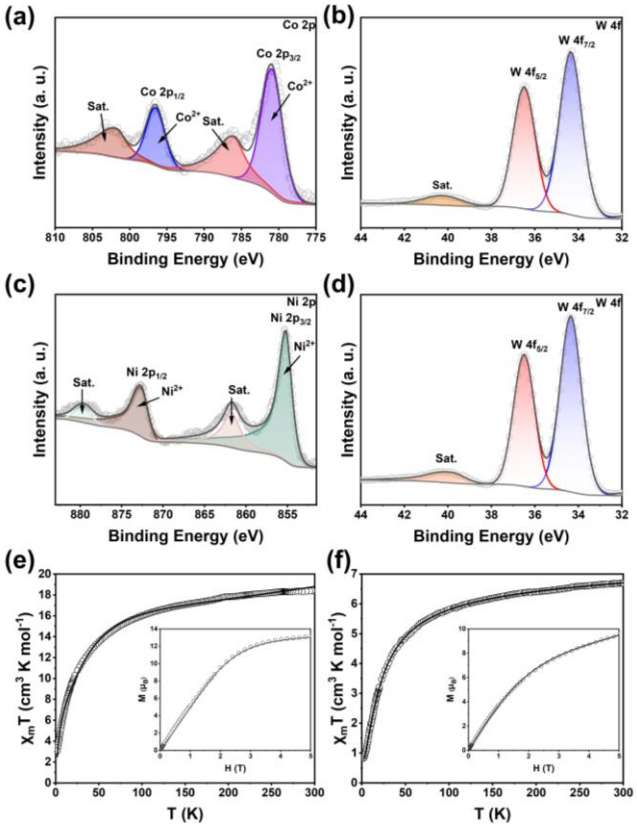

Figure 2. XPS spectra of Co_6-GeW_{12} in: (a) the Co 2p and (b) W 4f regions. XPS spectra of Ni_6-GeW_{12} in: (c) the Ni 2p and (d) W 4f regions. Thermal variation of the χ_mT product per formula unit for: (e) Co_6-GeW_{12} and (f) Ni_6-GeW_{12}. Insets show the isothermal magnetizations at 2 K. Solid lines are the best fit to the models.

A further confirmation of the oxidation state and the spin configuration of both cations is provided by the magnetic measurements of both compounds. As can be seen in Figure 2, the product of the molar magnetic susceptibility per formula unit (i.e., Ni_6 or Co_6) times the

temperature ($\chi_m T$) for Ni_6-GeW_{12} and Co_6-GeW_{12}, shows values at room temperature of around 6.7 and 18.4 cm^3 K mol^{-1}, respectively (i.e., around 1.1 and 3.1 cm^3 K mol^{-1} per Ni^{II} and Co^{II} ion). These values are the expected ones for one independent Ni^{II} ion with g = 2.12 and within the normal range observed for HS Co^{II} ions (2.8-3.4 cm^3 K mol^{-1}, depending on the orbital contribution of the $^4T_{1g}$ ground state of the HS Co^{II} ions).[48,49] When the samples are cooled, both compounds show progressive decreases when the temperature is decreased to reach values of 0.7 and 3.0 cm^3 K mol^{-1} at 2 K (Figure 2). This behavior confirms the existence of weak antiferromagnetic interactions in both compounds, although in Co_6-GeW_{12} the decrease may be also because of the existence of a spin-orbit coupling arising from the $^4T_{1g}$ ground state.[48,49]

The isothermal magnetization at 2 K for both compounds show also a very similar behaviour (insets in Figure 2) and confirm the presence of high spin Co^{II} ions in Co_6-GeW_{12}. Thus, the saturation value of 9.5 μ_B per formula unit for Ni^{II} derivatives is close to 11-12 μ_B (i.e., slightly below 2 μ_B per Ni^{II} ion, which is the expected value for an isolated Ni^{II} ion with g = 2, inset in Figure 2f). The Co^{II} derivative exhibits a saturation value close to 14 μ_B per formula unit (i.e., around 2.3 μ_B per Co^{II} ion, inset in Figure 2e). This value is below the expected one (3.0 μ_B) for a high spin S = 3/2 spin ground state with g = 2, since at 2 K only the lowest Kramers doublet (originating from the splitting of the $^4T_{1g}$ term because of the first order spin-orbit coupling) is populated, resulting in an effective spin ground state of 1/2 at very low temperatures. Assuming an S = 1/2 ground spin state, the calculated effective g value for the Co^{II} ions is around 4.6, very close to those observed for other isolated HS Co(II) complexes.[48,49]

Since the structure of both compounds shows the presence of M^{II} dimers with double -N-N- bridges which are further connected to other four dimers by pyrazine bridges (Figures S7 and S8), we have fitted the magnetic performances of both compounds to a dimer model with an

interdimer interaction (j, modelled with the mean field approximation) using the program PHI.[50] Additionally, we have included a zero field splitting (ZFS) parameter (D) for the Ni^{II} ions whereas for the Co^{II} ions we have also included a spin-orbit coupling (λ) and an orbital reduction factor (α) with the following Hamiltonian:[50]

$$\hat{H}= \alpha\lambda\hat{L}\cdot\hat{S}+\alpha^2 B_2^0\left[3\hat{L}^2-\hat{L}^2\right]+\mu_B\left(\alpha\hat{L}\cdot I+2\hat{S}\cdot I\right)\cdot\vec{B}-2J_{dim}\cdot\hat{S}_1\cdot\hat{S}_2$$

This Hamiltonian implies two identical magnetically coupled octahedral high spin Co^{II} ions with a spin-orbit coupling (λ) and an orbital reduction factor (α = κA). The distortions from the ideal symmetry of the Co^{II} ion are included with the crystal field parameters B_2^0 (with $D = 3B_2^0\theta_2$) to account for the axial distortion.

For both compounds the dimer model reproduces simultaneously the thermal variation of $\chi_m T$ and the isothermal magnetization in a very satisfactorily way (solid lines in Figure 2) with the following parameters: g = 2.188(2), J_{dim} = -10.50(3) cm^{-1}, j = -0.28(1) cm^{-1}, |D| = 6.2(1) cm^{-1} and a monomeric S = 1 impurity of 3.9(1) % for Ni_6-GeW_{12} (solid lines in Figure 2f) and α = -1.15(1), λ = -96(1) cm^{-1}, |D| = 11.7(3) cm^{-1}, J_{dim} = -0.67(1) cm^{-1} and j = -0.07(1) cm^{-1} for Co_6-GeW_{12} (solid lines in Figure 2e). As can be seen in both cases we obtain a weak antiferromagnetic intradimer coupling (J) through the double -N-N- bridges, in agreement with the weak couplings observed in other similar Ni^{II} and high spin Co^{II} dimers connected through similar double -N-N- triazole bridges.[51-55] Note that the sign of the ZFS parameter (D) cannot be determine from magnetic measurement on polycrystalline samples and that the D and J parameters may be correlated, precluding a precise determination of both, although the D values are within the normal range found for other Ni^{II} and high spin Co^{II} complexes. [56]

Subsequently, the band gap structure of the title compound was investigated. The UV-Vis analysis reveals a broad band in the 200-400 nm range for both compounds that can be ascribed

to the GeW_{12}. The formation of the transition metals complexes with the organic ligands and the GeW_{12} broadens the absorption range, giving rise to bands in the 400-800 nm range that can be attributed to the electron transfer among the metal cations and the GeW_{12} clusters (Figure S9a).[57] Thus, the insertion of the GeW_{12} units into the M^{II}-pzta complexes results in the formation of 3D-POMOFs which effectively expand the absorption range (Figure S9a). Furthermore, the Co_6-GeW_{12} derivative exhibits enhanced absorption in the 400-600 nm range, thereby facilitating the absorption of a greater amount of photons in this range.[58] The optical bandgap widths of both compounds have been obtained by UV-Vis DRS coupled with the Tauc-plots (Figure S9b). The bandgap widths of GeW_{12}, Co_6-GeW_{12} and Ni_6-GeW_{12} were calculated to be 3.57, 2.68 and 2.74 eV, respectively. These results indicate that the formation of the 3D-POMOFs can effectively reduce the forbidden bandwidth. Moreover, Co_6-GeW_{12} has a smaller bandgap width and, therefore, it requires less energy when excited by light, favoring its photocatalytic activity since it can absorb more photon energy (Figure S9b). The LUMO of GeW_{12}, Co_6-GeW_{12} and Ni_6-GeW_{12} were deduced from Mott-Schottky plots tests. The flat band potentials of GeW_{12}, Co_6-GeW_{12}, and Ni_6-GeW_{12} for Ag/AgCl are -0.19, -0.41, and -0.38 V, respectively (Figures S10-S12), corresponding to LUMO energy levels of 0.007, -0.213, and -0.183 V vs. NHE.[59] Combined with the band gap values, the HOMO of GeW_{12}, Co_6-GeW_{12} and Ni_6-GeW_{12} can be estimated to be 3.577, 2.467 and 2.557 eV *vs*. NHE, respectively (Figure S13). These values show that: (i) the conduction band potential of the parent POM GeW_{12} (0.007 V *vs*. NHE) does not satisfy the condition of photocatalytic decomposition of water for hydrogen production and (ii) the introduction of transition metals and POM increases the conduction band potential (due to the mixing of metal orbitals) so that Co_6-GeW_{12} and Ni_6-GeW_{12} satisfy the condition of photocatalytic decomposition of water for hydrogen production.

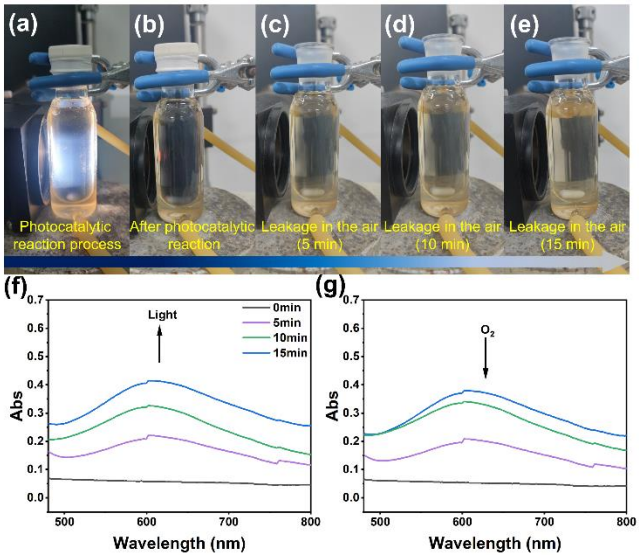

Figure 3. (a) HPB formation in Co_6-GeW_{12} under UV illumination; (b-e) HPB vanishing in Co_6-GeW_{12} photocatalytic system solution after exposure to O_2. (f) Evolution of the UV-vis diffuse reflectance spectra of Co_6-GeW_{12} with the UV light illumination time. (g) Evolution of the UV-vis diffuse reflectance spectra of Co_6-GeW_{12} with the O_2 exposure time.

We have studied the photocatalytic production of hydrogen using the two 3D-POMOFs Co_6-GeW_{12}, Ni_6-GeW_{12} and the pristine GeW_{12}, without the use of any noble metal co-catalysts, under a 500 W xenon lamp. The optimal experimental conditions were determined by conducting blank and comparative experiments, analyzing factors such as the type and concentration of sacrificial electron donor, as well as the range of irradiation wavelengths (Table S1).

When the light source was turned on, the solution of the catalytic system changed from colorless to blue after a period of irradiation, indicating the formation of reduced HPB anions (Figure 3a). The HPB color darkens with increasing the UV lamp irradiation time and the absorption band at 610 nm increases significantly (Figure 3f). This is due to the $W^{VI} \rightarrow W^{V}$ reduction process in the POM. After O_2 bubbling, the solution blue color vanished to a colorless suspension (Figures 3b-3e) and the absorption band at 610 nm gradually decreases, proving the

reversibility of the POM reduction (Figure 3g). In order to optimize the conditions for H_2 production, we have tested different sacrificial electron donors as lactic acid, methanol, triethanolamine (TEOA) and triethylamine (TEA). As can be seen in Figure 4a, the highest H_2 production, by far, is obtained for TEA. Consequently, we have performed all the catalytic studies with TEA as sacrificial electron donors.

In order to obtain the optimal solvent for H_2 evolution, we have tested different water-acetone mixtures. When pure water is used as solvent, the POM is not reduced to HPB and no hydrogen is produced (Figure 4b). This fact can be explained by the low water solubility of the TEA electron-sacrificing agent, that precludes the electron transfer with the catalyst. By changing the water: acetone ratio, we have found that the highest photocatalytic hydrogen production rate is obtained for an acetone: water ratio of 2 : 1 (Figure 4b). This results shows that acetone has an key role in the catalytic hydrogen production system since acetone enhances the contact between the electron donor (TEA) and the POM (electron acceptor), resulting in the formation of the HPB state. As expected, when we only use acetone as solvent, the lack of water as a source of H^+ results in the production of only trace amounts of H_2, most probably due to trace amounts of water in the acetone and/or the dehydrogenation of acetone (Figure 4b).

Subsequently, we have investigated the effect of the concentration of the sacrificial agent (TEA) on the photocatalytic system. We find a maximum photocatalytic hydrogen production rate for a TEA concentration of 10 % (Figure 4c). This results suggests that for low TEA concentrations the sacrificial agent is not able to restore all the holes left by the photoexcited electrons in the catalyst, whereas too much sacrificial agent would block the active sites of the catalyst, leading to a decrease in the photocatalytic hydrogen production rate.

Once the previously mentioned variables were optimized (solvent, electron donor and its concentration), we have measured the H_2 production using, in a typical experiment, a 20 mL solution of the photocatalytic system, consisting of 5 mg of photocatalyst, acetone: water ratio of 2: 1 (v/v) and 10 % TEA ($v/v_{solution}$) as a sacrificial agent. The reaction was carried out for 6 hours under the aforementioned conditions. Co_6-GeW_{12} exhibited a significantly higher hydrogen production rate of 13.7 mmol g^{-1} h^{-1}, more than ten times higher than Ni_6-GeW_{12}, which achieved a rate of 1.24 mmol g^{-1} h^{-1} (Figure 4d).

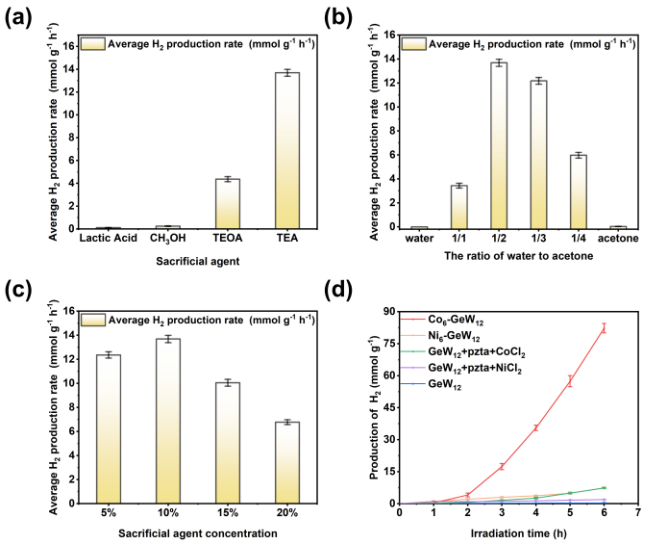

Figure 4. Comparison of hydrogen production performance of photocatalysts under different conditions: (a) type of sacrificial agent; (b) solvent concentration; (c) sacrificial agent concentration and (d) performance comparison of different catalysts. Figures a, b, c and d, present data as mean ± SD (n = 3).

Additionally, the two 3D-POMOFs exhibit different behavior during the photocatalytic reactions. Thus, after 2 hours of light exposure, Co_6-GeW_{12} formed the heteropoly blue POM (HPB, Figure 5f), indicative of a reduction of the POM.[36,43] In contrast, Ni_6-GeW_{12} did not exhibit the HPB formation after light exposure (Figure 5e). This different behavior may be the reason for the so different performances of these two 3D-POMOFs.

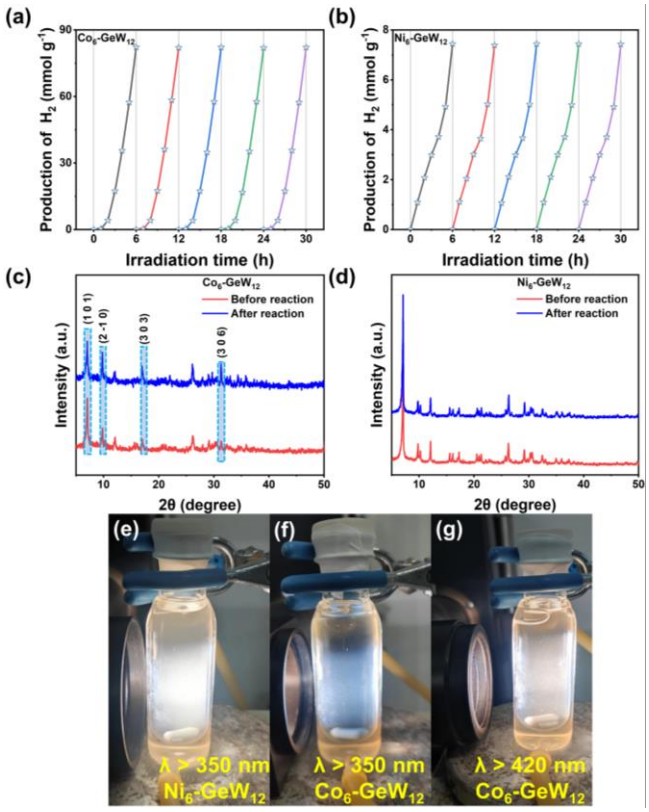

Figure 5. Cycling tests for (a) Co_6-GeW_{12} and (b) Ni_6-GeW_{12}. X-ray diffraction patterns of (c) Co_6-GeW_{12} and (d) Ni_6-GeW_{12} before and after illumination. Photocatalytic solutions of (e) Ni_6-GeW_{12} and (f-g) Co_6-GeW_{12} under different irradiation.

The two 3D-POMOF photocatalysts exhibit remarkable cycling stability, with catalytic activities close to the initial value even after five consecutive cycles within a 30 h time frame (Figures 5a and 5d). In addition, X-Ray diffraction experiments reveal that the Ni_6-GeW_{12} photocatalyst maintains its structural stability after the photocatalytic tests (Figure 5d). In contrast, the characteristic peaks of the Co_6-GeW_{12} photocatalysts undergo significant changes, with a decrease in the diffraction peak of the (1 0 1) plane and a significant increase in those of the (2 -1 0), (3 0 3) and (3 0 6) planes (Figure 5c). This change in the X-ray diffractogram suggests that the Co_6-GeW_{12} catalyst suffers a partial structural transformation during the catalytic cycle in the organic alkaline solution. This structural change allows the transfer of

electrons from TEA to POM, forming the HPB state during the photocatalytic process. This structural differences explains the different behavior of the two 3D-POMOFs during photocatalytic experiments. The lower ligand field stabilization energy (LFSE) of Co^{II} complexes compared to Ni^{II} complexes explains their structural etching.[60] In addition, there was no significant difference between the IR after and before the reaction, indicating the good stability of the two catalysts (Figure S14). To further demonstrate phase purity, we analyzed in the 5-50 range using software (PowderCell 2.3) that simulates powder spectra and allows for rapid Rietveld refinement based on single-crystal data. As shown in (Figure S15), by fitting both samples before and after the reaction to the simulated data, both have a good match. The variability in the fitted data stems from the difference in peak intensities, which is further evidence that there is no additional phase in the samples.

Electrochemical impedance spectroscopy (EIS) shows that Co_6-GeW_{12} has a slightly lower impedance than Ni_6-GeW_{12} and both have significantly lower impedances than the pristine GeW_{12} POM. (Figure S16). The photoluminescence (PL) spectra of Co_6-GeW_{12} and Ni_6-GeW_{12}, recorded with an excitation wavelength of 360 nm, show that both compounds have better photogenerated electron hole separation rates compared to the pristine POM (Figure S17).[61] As shown in Figure S18, the EPR signals of the catalysts were significantly different when 2,2,6,6-tetramethylpiperidinooxy (TEMPO) was used as the electron trapping agent, and the weaker EPR signals indicated that more photogenerated electrons were generated during the photocatalytic process to be trapped by the TEMPO.[62] Notably, Co_6-GeW_{12} mixed with TEMPO showed the lowest EPR signal under irradiation (Co_6-GeW_{12} < Ni_6-GeW_{12} < GeW_{12}), which confirms its ability to produce the highest concentration of photogenerated electrons in all samples. Additionally, Co_6-GeW_{12} shows a higher photocurrent intensity than Ni_6-GeW_{12} and

both compounds show much higher photocurrent intensity than the pristine GeW_{12}, as clearly shown by the photocurrent response tests (Figure S19). This result indicates the Co_6-GeW_{12} has the best photogenerated electron hole separation rate. In summary, all the previous results support the much better photocatalytic H_2 production shown by Co_6-GeW_{12}. Moreover, the linear sweep voltammetry (LSV) shows that Co_6-GeW_{12} has a lower overpotential for H^+ activation than Ni_6-GeW_{12} (and both POMOF much lower than the pristine GeW_{12} POM, Figure S20), in agreement with the much higher photocatalytic H_2 production shown by Co_6-GeW_{12}. A promising material for photocatalytic HER should exhibit not only high electron transfer ability but also moderate H adsorption ability.

Therefore, we have also examined the free energy change for H adsorption on Ni_2-POM and Co_2-POM models, with H adsorption on Ni and Co sites. As shown in Figure S21, the adsorption of H on Co (ΔG_{H^*} = 0.02 eV) is much less energetic than on Ni (ΔG_{H^*} = 0.42 eV), indicating that Co_2-POM has a better catalytic capacity for hydrogen evolution.[63,64]

DFT calculations were explored based on the cluster model Co_2/Ni_2-POM shown in Figure 6a to explore the electron storage and transfer behavior in the photocatalytic process. The orbital energies and compositions for fully oxidized Co_2-POM and Ni_2-POM are compared in Figure 6b.In agreement with the experimental trend, the Co_2-POM cluster exhibits a smaller band gap than the Ni_2-POM cluster, while the orbital distribution is almost the same in both clusters (Figure 6b). As can be seen in the central part of Figure 6b, the distribution of the highest occupied molecular orbital (HOMO) and the lowest unoccupied molecular orbital (LUMO) is completely different. Thus, the LUMO is totally localized on the W-5d orbitals of the POM whereas the HOMO is totally localized on the Co_2 and Ni_2 complexes. These electronic distributions imply that the photogenerated electrons will initially be stored in the POM fraction

of the Co_2-POM unit resulting in the corresponding photo-reduced POMs: $(POM)^{n-}$. The spin density and LUMO distributions of the $2e^-$, $4e^-$ and $6e^-$ reduced Co_2-POM cluster are shown in Figure 6c. As observed in the initial Co_2-POM cluster, the LUMO of the $2e^-$-reduced Co_2-POM $(Co_2\text{-POM})^{2e-}$ is still localized on the POM framework and the spin density analysis demonstrates that the two added electrons are mainly located on the POM, responsible of the characteristic blue color in the HPB state. However, when the Co_2-POM cluster is further reduced by four or six electrons to form $(Co_2\text{-POM})^{4e-}$ and $(Co_2\text{-POM})^{6e-}$ species, the LUMO distribution changes from the POM to the Co_2 site (Figure 6c). The successive reduction of the Co_2-POM cluster indicates an electron transfer from the POM fragment to the Co_2 complex could take place under continuous light excitation. This results agree with the experimental data that show the formation of HPB state in the Co_6-GeW_{12} POMOF during the catalytic reaction and explains the electron transfer role played by the Co^{II} complex in the catalytic process. Although the LUMO and HOMO distributions of Ni-POM after $4e^-$ reduction were similar to those of Co-POM (Figure S22), the HPB phenomenon was not observed during the 6 h photocatalytic experiment. We hypothesized two possible reasons for this phenomenon in line with the results of DFT calculations and measurements of XRD of the samples post reaction: i) Due to the electronic structure of the Ni^{II} ion being in a steady state, the higher fluorescence intensity suggesting that the photogenerated electrons and holes of Ni_6-GeW_{12} are more readily complexed, and the wider bandgap suggesting that greater energy is required for the photoexcitation of Ni_6-GeW_{12}. This makes it difficult for Ni^{II} to meet the $4e^-$ photogenerated reduction requirements when transferring electrons to POM; ii) The electronic structure of Ni^{II} ion is $t_{2g}^6e_g^2$ as a stabilized structure which means that Ni^{II} ion has a higher LFSE compared to Co^{II} ion ($t_{2g}^5e_g^2$).[60] The higher LFSE of Ni^{II} induces greater structural stability in Ni-POM

compared to Co-POM, which impedes electron transfer from the sacrificial agent (TEA) to the POM.

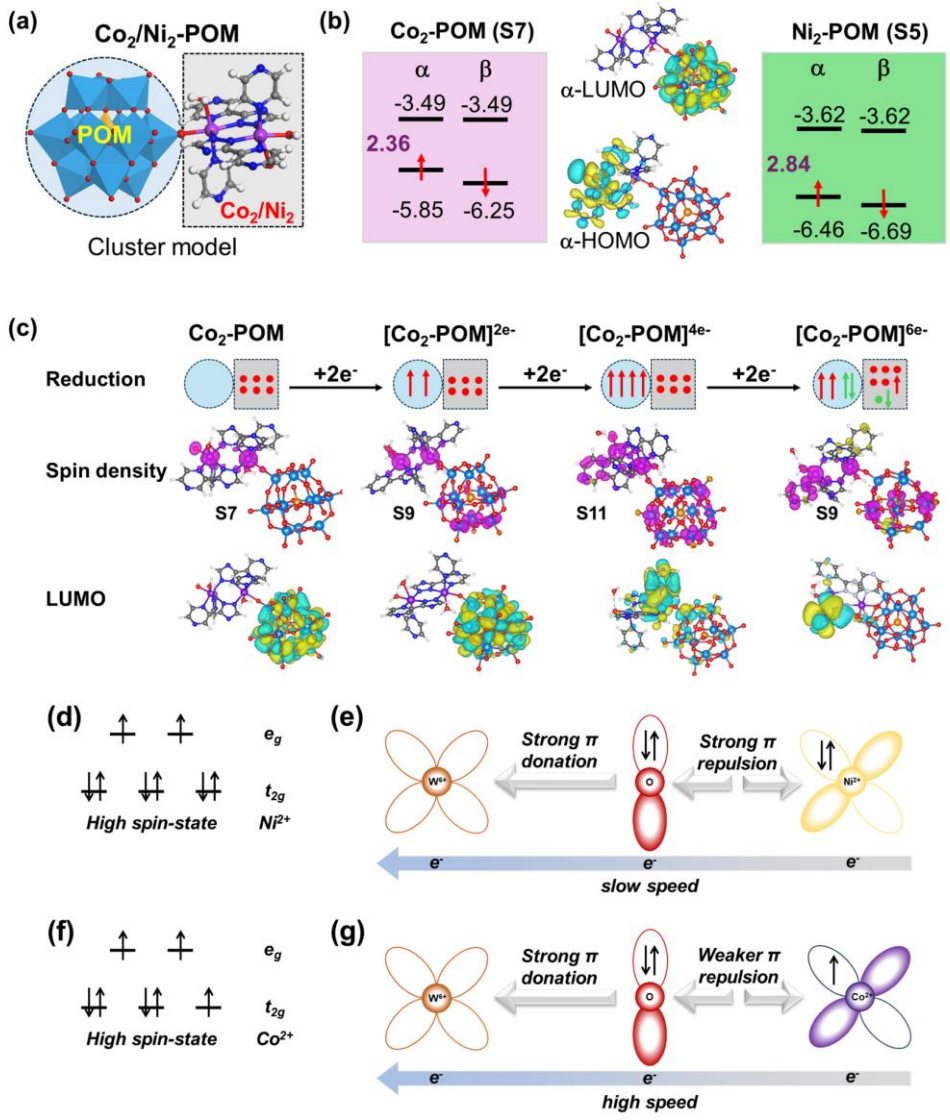

Figure 6. (a) The computational cluster model. (b) Computed orbital energies (values in eV) and molecular orbital distribution of HOMO and LUMO involved in Co_2-POM and Ni_2-POM. (c) Unpaired electron distribution, spin density and LUMO distribution for Co_2-POM with different reduction degrees. (d and f) Electronic structure of the high-spin states Co^{2+} and Ni^{2+}. (e and g) Electronic interactions in the production of heteropoly blue.

To better explain the photocatalytic reaction mechanism, we have studied the electronic structures of Co^{II} and Ni^{II} in the high-spin state. As shown in Figures 6d and 6f, the $e_g(\sigma)$ orbitals of octahedral Ni^{II} and HS Co^{II} have two unpaired electrons. The difference between both ions is found in the $t_{2g}(\pi)$ orbitals: Co^{II} has an unpaired electron in one of these three $t_{2g}(\pi)$ orbitals that allows the electron transfer through the π-bonds between the O atoms of the POM. In contrast, the $t_{2g}(\pi)$ orbitals of Ni^{II} are fully filled with electrons, precluding the electron transfer with the O atoms through the π-bonds. In this case, the electrons can only be transferred through the $e_g(\sigma)$ orbitals. When the POM is not photo-reduced, the 5d orbital in the center of W^{VI} is empty and there is a weak π-electron repulsion between the Co-O bonds, therefore, the photogenerated electrons tend to go from Co^{II} to W^{VI}. According to the electron coupling mechanism for M-O-W (M = Ni or Co), both Ni^{II} and Co^{II} can transfer part of the electrons to W^{VI}, but the electron transfer mode is different, and the electron transfer efficiency of Co_6-GeW_{12} is much higher (Figures 6e and 6g).[65-68] This electrons transfer is completely reversed when the POM undergoes a photoreduction of $4e^-$, in agreement with the results of DFT calculations.

Based on the above data and calculations, we propose the mechanism displayed in Figure 7 for hydrogen production by photocatalysis Co_6-GeW_{12}. After illumination, the photogenerated electrons in the $[Co^{II}_6(pzta)_6(H_2O)_4(OH)_2]_n^{4n+}$ are transferred to the GeW_{12} *via* molecular junctions. TEA acts as an electron donor to transfer electrons to GeW_{12}, reducing the GeW_{12} to produce the HPB state. Photogenerated electrons trapped in the W centers of the HPB absorb visible light and are transferred to the Co^{II} centers. The reduced Co centers transfer the excess electrons to H^+ in water to produce H_2. After transferring the electrons to the Co center, the HPB species reverts to its colorless oxidized state, completing the photocatalytic cycle. The photogenerated holes generated during photocatalysis are filled by sacrificial agents.[36,38,69]

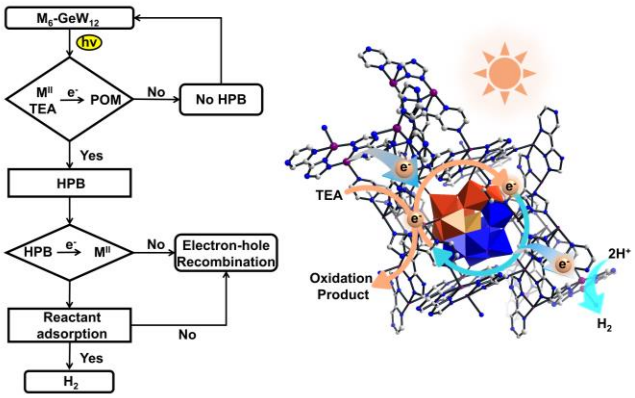

Figure 7. Co_6-GeW_{12} photocatalytic mechanism.

CONCLUSIONS

In this study, we have successfully synthesized two 3D-POMOFs with molecular junction structures, Co_6-GeW_{12} and Ni_6-GeW_{12}, by introducing Ni^{II} and high-spin Co^{II} ions into the POMOF structure. We have thoroughly investigated their differences in photocatalytic hydrogen evolution. The experimental results reveal that Co_6-GeW_{12} exhibits higher electron transfer efficiency and produces a heteropoly blue (HPB) state during the photocatalytic process, significantly enhancing its photocatalytic activity. In contrast, Ni_6-GeW_{12} do not form the HPB state, resulting in lower catalytic performance. This disparity is attributed to the differences in electronic structure between the two metal ions.

Author Contributions

‡W. Z. Sun and B. Zhao contributed equally to this work.

Notes

The authors declare no competing financial interest.

SUPPORTING INFORMATION

A Detailed information regarding the experimental methods; characterization analysis; DFT calculations; and crystal data.

ACKNOWLEDGMENT

This work was financially supported by the National Science Foundation of China (22171059) and the Major Research Plan National Natural Science Foundation of China (92061102). It is also financially supported by the Foundation of Jilin Educational Committee (grant no. JJKH20231298KJ), and Natural Scientific Foundation of Jilin Province Science and Technology Department (grant no. 20230101032JC). This study forms part of the Advanced Materials program and was supported by the Spanish MCIN with funding from European Union NextGeneration EU (PRTR- C17.I1) and the Generalitat Valenciana (project MFA-2022-057). We also thank the Grant PID2021-125907NB-I00 funded by MCIN/AEI/10.13039/501100011033 and by "ERDF A way of making Europe" and project CIPROM-2022-060 from the Generalitat Valenciana, for financial support.

REFERENCES

1. Gong, J.; Li, C.; Wasielewski, M. R., Advances in solar energy conversion. *Chem. Soc. Rev.* **2019,** *48* (7), 1862-1864.

2. Jiao, L.; Dong, Y.; Xin, X.; Wang, R.; Lv, H., Three-in-one: achieving a robust and effective hydrogen-evolving hybrid material by integrating polyoxometalate, a photo-responsive metal–organic framework, and in situ generated Pt nanoparticles. *J. Mater. Chem. A* **2021,** *9* (35), 19725-19733.

3. Lv, H.; Guo, W.; Wu, K.; Chen, Z.; Bacsa, J.; Musaev, D. G.; Geletii, Y. V.; Lauinger, S. M.; Lian, T.; Hill, C. L., A noble-metal-free, tetra-nickel polyoxotungstate catalyst for efficient photocatalytic hydrogen evolution. *J. Am. Chem. Soc.* **2014,** *136* (40), 14015-14018.

4. Lv, H.; Song, J.; Zhu, H.; Geletii, Y. V.; Bacsa, J.; Zhao, C.; Lian, T.; Musaev, D. G.; Hill, C. L., Visible-light-driven hydrogen evolution from water using a noble-metal-free polyoxometalate catalyst. *J. Catal.* **2013,** *307*, 48-54.

5. Fujishima, A.; Honda, K., Electrochemical photolysis of water at a semiconductor electrode. *Nature* **1972,** *238* (5358), 37-38.

6. Sun, W.; Pang, H.; Khan, S. U.; Yang, R.; Wu, Q.; Ma, H.; Au, C. M.; Sun, W.; Wang, X.; Yang, G.; Yu, W. Y., Highly Efficient Photocatalysts: Polyoxometalate Synthons Enable Tailored CdS-MoS_2 Morphologies and Enhanced H_2 Evolution. *ACS Appl. Mater. Interfaces* **2023,** *15* (29), 35611-35621.

7. Chandrasekaran, S.; Yao, L.; Deng, L.; Bowen, C.; Zhang, Y.; Chen, S.; Lin, Z.; Peng, F.; Zhang, P., Recent advances in metal sulfides: from controlled fabrication to electrocatalytic, photocatalytic and photoelectrochemical water splitting and beyond. *Chem. Soc. Rev.* **2019,** *48* (15), 4178-4280.

8. Zhang, F.-M.; Sheng, J.-L.; Yang, Z.-D.; Sun, X.-J.; Tang, H.-L.; Lu, M.; Dong, H.; Shen, F.-C.; Liu, J.; Lan, Y.-Q., Rational Design of MOF/COF Hybrid Materials for Photocatalytic H_2 Evolution in the Presence of Sacrificial Electron Donors. *Angew. Chem. Int. Ed.* **2018,** *57* (37), 12106-12110.

9. Zhang, Y.; Wu, Q.; Seow, J. Z. Y.; Jia, Y.; Ren, X.; Xu, Z. J., Spin states of metal centers in electrocatalysis. *Chem. Soc. Rev.* **2024,** *53* (16), 8123-8136.

10. Pei, C.; Kim, M. C.; Li, Y.; Xia, C.; Kim, J.; So, W.; Yu, X.; Park, H. S.; Kim, J. K., Electron Transfer‐Induced Metal Spin-Crossover at $NiCo_2S_4/ReS_2$ 2D-2D Interfaces for Promoting pH-universal Hydrogen Evolution Reaction. *Adv. Funct. Mater.* **2022,** *33* (4), 2210072.

11. Xia, C.; Liang, H.; Zhu, J.; Schwingenschlögl, U.; Alshareef, H. N., Active Edge Sites Engineering in Nickel Cobalt Selenide Solid Solutions for Highly Efficient Hydrogen Evolution. *Adv. Energy Mater.* **2017,** *7* (9), 1602089.

12. Liu, Y.; Hua, X.; Xiao, C.; Zhou, T.; Huang, P.; Guo, Z.; Pan, B.; Xie, Y., Heterogeneous Spin States in Ultrathin Nanosheets Induce Subtle Lattice Distortion To Trigger Efficient Hydrogen Evolution. *J. Am. Chem. Soc.* **2016,** *138* (15), 5087-5092.

13. Sun, K.; Huang, Y.; Wang, Q.; Zhao, W.; Zheng, X.; Jiang, J.; Jiang, H.-L., Manipulating the Spin State of Co Sites in Metal–Organic Frameworks for Boosting CO_2 Photoreduction. *J. Am. Chem. Soc.* **2024,** *146* (5), 3241-3249.

14. Miras, H. N.; Yan, J.; Long, D. L.; Cronin, L., Engineering polyoxometalates with emergent properties. *Chem. Soc. Rev.* **2012,** *41* (22), 7403-7430.

15. Wang, S. S.; Yang, G. Y., Recent advances in polyoxometalate-catalyzed reactions. *Chem. Rev.* **2015,** *115* (11), 4893-4962.

16. Pope, M. T.; Müller, A., Polyoxometalate Chemistry: An Old Field with New Dimensions in Several Disciplines. *Angew. Chem. Int. Ed.* **1991,** *30* (1), 34-48.

17. Li, J. S.; Sang, X. J.; Chen, W. L.; Zhang, L. C.; Zhu, Z. M.; Ma, T. Y.; Su, Z. M.; Wang, E. B., Enhanced Visible Photovoltaic Response of TiO_2 Thin Film with an All-Inorganic Donor-Acceptor Type Polyoxometalate. *ACS Appl. Mater. Interfaces* **2015,** *7* (24), 13714-13721.

18. Song, Y.; Li, Z.; Zhu, Y.; Feng, X.; Chen, J. S.; Kaufmann, M.; Wang, C.; Lin, W., Titanium Hydroxide Secondary Building Units in Metal-Organic Frameworks Catalyze Hydrogen Evolution under Visible Light. *J. Am. Chem. Soc.* **2019,** *141* (31), 12219-12223.

19. James, S. L., Metal-organic frameworks. *Chem. Soc. Rev.* **2003,** *32* (5), 276-288.

20. Yang, M.; Wang, X.; Gómez‐García, C. J.; Jin, Z.; Xin, J.; Cao, X.; Ma, H.; Pang, H.; Tan, L.; Yang, G.; Kan, Y., Efficient Electron Transfer from an Electron-Reservoir Polyoxometalate to Dual‐Metal‐Site Metal‐Organic Frameworks for Highly Efficient Electroreduction of Nitrogen. *Adv. Funct. Mater.* **2023,** *33* (28), 2214495.

21. Zhou, H. C.; Long, J. R.; Yaghi, O. M., Introduction to metal-organic frameworks. *Chem. Rev.* **2012,** *112* (2), 673-674.

22. Liu, Y.; Tang, C.; Cheng, M.; Chen, M.; Chen, S.; Lei, L.; Chen, Y.; Yi, H.; Fu, Y.; Li, L., Polyoxometalate@Metal–Organic Framework Composites as Effective Photocatalysts. *ACS Catal.* **2021,** *11* (21), 13374-13396.

23. Wei, X.; Jiang, Y.; Ma, Y.; Liao, H.; Dai, S.; An, P.; Wang, Z.-Q.; Gong, X.-Q.; Hou, Z., High Performance Polyoxometalate-Stabilizing Pt Nanocatalysts for Quinoline Hydrogenation with Water-Mediated Dynamic Hydrogen. *ACS Catal.* **2024,** *14* (7), 5344-5355.

24. Taira, N.; Yamauchi, K.; Sakai, K., Intracluster O–O Coupling Pathway Evidenced for an Anderson-Type Single-Cobalt Polymolybdate Water Oxidation Catalyst. *ACS Catal.* **2023,** *13* (5), 3211-3223.

25. Hu, Q.; Zhou, H.; Ding, Y.; Wågberg, T.; Han, X., Advances in Bridging Homogeneous and Heterogeneous Water Oxidation Catalysis by Insolubilized Polyoxometalate Clusters. *ACS Catal.* **2024,** *14* (8), 5898-5910.

26. Geng, W.; Zhang, D.; Zhen, N.; Du, J.; Dong, J.; Liu, C.; Chen, S.-L.; Chi, Y.; Hu, C., Electroreductive C–C Coupling of Furfural to Jet Fuel Precursors in Neutral Media via Synergistic Catalysis of the Polyoxotungstate and Cu Complex. *ACS Catal.* **2024,** *14* (13), 10040-10052.

27. Chi, M.; Zeng, Y.; Lang, Z.-L.; Li, H.; Xin, X.; Dong, Y.; Fu, F.; Yang, G.-Y.; Lv, H., Molecular Orbital Engineering of Mixed-Addenda Polyoxometalates Boosts Light-Driven Hydrogen Evolution Activity. *ACS Catal*. **2024,** *14* (7), 5006-5015.

28. Liao, J.-P.; Zhang, M.; Huang, P.; Dong, L.-Z.; Ma, T.-T.; Huang, G.-Z.; Liu, Y.-F.; Lu, M.; Li, S.-L.; Lan, Y.-Q., Flexible Units Induced Three-Dimensional Covalent Organic Frameworks with a Heteromotif Molecular Junction for Photocatalytic H_2O_2 Production. *ACS Catal.* **2024,** *14* (6), 3778-3787.

29. Li, X. X.; Zhang, L.; Liu, J.; Yuan, L.; Wang, T.; Wang, J. Y.; Dong, L. Z.; Huang, K.; Lan, Y. Q., Design of Crystalline Reduction-Oxidation Cluster-Based Catalysts for Artificial Photosynthesis. *JACS Au* **2021,** *1* (8), 1288-1295.

30. Zhang, L.; Li, R. H.; Li, X. X.; Liu, J.; Guan, W.; Dong, L. Z.; Li, S. L.; Lan, Y. Q., Molecular oxidation-reduction junctions for artificial photosynthetic overall reaction. *Proc. Natl. Acad. Sci U S A* **2022,** *119* (40), e2210550119.

31. Li, X. X.; Hong, X. X.; Liao, Z. Y.; Zhang, L.; Li, R. H.; Zeng, Y.; Liu, Y.; Li, S. L.; Lan, Y. Q., Tri-functional molecular junction photocatalyst for cascade synthesis of N-benzylideneaniline derivatives. *Sci. Bull. (Beijing)* **2024,** *69* (23), 3661-3665.

32. Wang, H.; Hamanaka, S.; Nishimoto, Y.; Irle, S.; Yokoyama, T.; Yoshikawa, H.; Awaga, K., In operando X-ray absorption fine structure studies of polyoxometalate molecular cluster batteries: polyoxometalates as electron sponges. *J. Am. Chem. Soc.* **2012**, *134* (10), 4918-4924.

33. Nishimoto, Y.; Yokogawa, D.; Yoshikawa, H.; Awaga, K.; Irle, S., Super-Reduced Polyoxometalates: Excellent Molecular Cluster Battery Components and Semipermeable Molecular Capacitors. *J. Am. Chem. Soc.* **2014**, *136* (25), 9042-9052.

34. Anandan, S.; Yoon, M., Heteropolyacid-encapsulated TiHY zeolite as an inorganic photosynthetic reaction center mimicking the plant systems. *J. Photochem. Photobiol. A: Chem.* **2003,** *160* (3), 181-184.

35. Du, J.; Ma, Y.-Y.; Cui, W.-J.; Zhang, S.-M.; Han, Z.-G.; Li, R.-H.; Han, X.-Q.; Guan, W.; Wang, Y.-H.; Li, Y.-Q.; Liu, Y.; Yu, F.-Y.; Wei, K.-Q.; Tan, H.-Q.; Kang, Z.-H.; Li, Y.-G., Unraveling photocatalytic electron transfer mechanism in polyoxometalate-encapsulated metal-organic frameworks for high-efficient CO_2 reduction reaction. *Appl. Catal. B-Environ.* **2022,** *318*, 121812.

36. Li, B.; Yu, X.; Pang, H.; Shen, Q.; Hou, Y.; Ma, H.; Xin, J., Rational regulation of transition metals in polyoxometalate hybrids without noble metal assistance for efficient light-driven H_2 production. *Chem. Commun.* **2020,** *56* (52), 7199-7202.

37. Li, S.; Liu, S.; Liu, S.; Liu, Y.; Tang, Q.; Shi, Z.; Ouyang, S.; Ye, J., Ta_{12}/Ta_{16} cluster-containing polytantalotungstates with remarkable photocatalytic H_2 evolution activity. *J. Am. Chem. Soc.* **2012,** *134* (48), 19716-19721.

38. Liu, Y.; Liu, S.; He, D.; Li, N.; Ji, Y.; Zheng, Z.; Luo, F.; Liu, S.; Shi, Z.; Hu, C., Crystal Facets Make a Profound Difference in Polyoxometalate-Containing Metal-Organic Frameworks as Catalysts for Biodiesel Production. *J. Am. Chem. Soc.* **2015,** *137* (39), 12697-12703.

39. Deposition numbers 2406920 (for **Co_6-GeW_{12}**) and 2406921 (for **Ni_6-GeW_{12}**), contain the supplementary crystallographic data for this paper. These data are provided free of charge by the joint Cambridge Crystallographic Data Centre and Fachinformationszentrum Karlsruhe Access Structures service.

40. Chen, J.-X.; Lan, T.-Y.; Huang, Y.-B.; Wei, C.-X.; Li, Z.-S.; Zhang, Z.-C., Hydrothermal synthesis, crystal structure and properties of a 3D-framework polyoxometalate assembly: [Ag(4,4'-bipy)](OH){[Ag(4,4'-bipy)]$_2$[PAg$W_{12}O_{40}$]}·3.5H_2O. *J. Solid State Chem.,* **2006,** *179* (6), 1904-1910.

41. Wu, C. D.; Lu, C. Z.; Zhuang, H. H.; Huang, J. S., Hybrid coordination polymer constructed from beta-octamolybdates linked by quinoxaline and its oxidized product benzimidazole coordinated to binuclear copper(I) fragments. *Inorg. Chem.* **2002,** *41* (22), 5636-5637.

42. Tan, P.; Chen, B.; Xu, H.; Cai, W.; He, W.; Ni, M., In-situ growth of Co_3O_4 nanowire-assembled clusters on nickel foam for aqueous rechargeable Zn-Co_3O_4 and Zn-air batteries. *Appl. Catal. B-Environ.* **2019,** *241*, 104-112.

43. Dou, S.; Tao, L.; Huo, J.; Wang, S.; Dai, L., Etched and doped Co9S8/graphene hybrid for oxygen electrocatalysis. *Energy Environ. Sci.* **2016,** *9* (4), 1320-1326.

44. Zhang, R.; Lu, Y.; Wei, L.; Fang, Z.; Lu, C.; Ni, Y.; Xu, Z.; Tao, S.; Li, P., Synthesis and conductivity properties of $Gd_{0.8}Ca_{0.2}BaCo_2O_5^{+\delta}$ double perovskite by sol–gel combustion. *J. Mater. Sci.-Mater. Electron.* **2015,** *26* (12), 9941-9948.

45. Wu, L. L.; Wang, Q. S.; Li, J.; Long, Y.; Liu, Y.; Song, S. Y.; Zhang, H. J., Co_9S_8 Nanoparticles‐Embedded N/S‐Codoped Carbon Nanofibers Derived from Metal‐Organic Framework‐Wrapped CdS Nanowires for Efficient Oxygen Evolution Reaction. *Small* **2018,** *14* (20), 1704035.

46. Wu, K.-H.; Liu, Y.; Tan, X.; Liu, Y.; Lin, Y.; Huang, X.; Ding, Y.; Su, B.-J.; Zhang, B.; Chen, J.-M.; Yan, W.; Smith, S. C.; Gentle, I. R.; Zhao, S., Regulating electron transfer over asymmetric low-spin Co(II) for highly selective electrocatalysis. *Chem. Catal.* **2022,** *2* (2), 372-385.

47. Pang, X.; Zhao, H.; Huang, Y.; Luo, B.; Bai, H.; Fan, W., Electrochemically induced NiOOH/Ag^+ active species for efficient oxidation of 5-hydroxymethylfurfural. *Appl. Surf. Sci.* **2023,** *608*, 155152.

48. Lloret, F.; Julve, M.; Cano, J.; Ruiz-García, R.; Pardo, E., Magnetic properties of six-coordinated high-spin cobalt(II) complexes: Theoretical background and its application. *Inorg. Chim. Acta* **2008,** *361* (12-13), 3432-3445.

49. Shi, Z.; Peng, J.; Gómez-García, C. J.; Benmansour, S.; Gu, X., Influence of metal ions on the structures of Keggin polyoxometalate-based solids: Hydrothermal syntheses, crystal structures and magnetic properties. *J. Solid State Chem.* **2006,** *179* (1), 253-265.

50. Chilton, N. F.; Anderson, R. P.; Turner, L. D.; Soncini, A.; Murray, K. S., PHI: A powerful new program for the analysis of anisotropic monomeric and exchange-coupled polynuclear d- and f-block complexes. *J. Comput. Chem.* **2013,** *34* (13), 1164-1175.

51. Li, H.; Zhang, N.; Liu, J.; Su, M.; Zeng, S.; Xu, Z., Synthesis and magnetic properties of chiral molecular magnet regulated by terminal coordination groups. *Polyhedron* **2018,** *154*, 108-113.

52. Martín-Ramos, P.; Silva, M. R.; de A. e Silva, J.; Martins, N. D.; Yuste-Vivas, C.; Pereira da Silva, P. S.; Sobral, A. J. F. N.; Pereira, L. C. J., Synthesis, structure and magnetic properties of mono-, dinuclear and polymeric compounds of transition metals with 4-amino-3,5-di-2-pyridyl-4H-1,2,4-triazole. *J. Mol. Struct.* **2016,** *1108*, 278-287.

53. Laachir, A.; Guesmi, S.; Ketatni, E. M.; Saadi, M.; El Ammari, L.; Mentré, O.; Esserti, S.; Faize, M.; Bentiss, F., A new homobimetallic cobalt(II) complex based on the tetradentate 3,5-bis(2-pyridyl)-1H-1,2,4-triazole ligand: Synthesis, crystal structure, Hirshfeld analysis, spectroscopic characterization, magnetic properties and antimicrobial activities. *Polyhedron* **2020,** *189*, 114722.

54. Zhong, L.; Xie, S.-F.; He, J.-Q.; Zhong, Q.-S.; Yang, M.; Chen, W.-B.; Dong, W., Syntheses, structures, magnetism and electrocatalytic oxygen evolution for four cobalt, manganese and copper complexes with dinuclear, 1D and 3D structures. *Dalton Trans.* **2019,** *48* (10), 3467-3475.

55. Pang, X.; Liu, J.; Wei, G.; Shi, D.; Bian, H.; Liu, H.; Yao, D.; Li, H.; Huang, F., Tracking the Formation of a Series of Co_n (n=2, 6, 8) Clusters from Linear Co_3 Precursor Clusters by Optimizing the Reaction Conditions. *ChemistrySelect* **2018,** *3* (27), 7830-7835.

56. Boča, R., Zero-field splitting in metal complexes. *Coord. Chem. Rev.* **2004,** *248* (9-10), 757-815.

57. Sun, W.; He, C.; Liu, T.; Duan, C., Synergistic catalysis for light-driven proton reduction using a polyoxometalate-based Cu-Ni heterometallic-organic framework. *Chem. Commun.* **2019,** *55* (26), 3805-3808.

58. Yonesato, K.; Ito, H.; Itakura, H.; Yokogawa, D.; Kikuchi, T.; Mizuno, N.; Yamaguchi, K.; Suzuki, K., Controlled Assembly Synthesis of Atomically Precise Ultrastable Silver Nanoclusters with Polyoxometalates. *J. Am. Chem. Soc.* **2019,** *141* (50), 19550-19554.

59. Xiao, X.; Lin, S.; Zhang, L.; Meng, H.; Zhou, J.; Li, Q.; Liu, J.; Qiao, P.; Jiang, B.; Fu, H., Constructing Pd-N interactions in Pd/g-C_3N_4 to improve the charge dynamics for efficient photocatalytic hydrogen evolution. *Nano Res.* **2021,** *15* (4), 2928-2934.

60. Liu, H.; Silva, W. C.; Santana Goncalves de Souza, L.; Veiga, A. G.; Seixas, L.; Fujisawa, K.; Kahn, E.; Zhang, T.; Zhang, F.; Yu, Z.; Thompson, K.; Lei, Y.; de Matos, C. J. S.;

Rocco, M. L. M.; Terrones, M.; Grasseschi, D., 3d transition metal coordination on monolayer MoS_2: a facile doping method to functionalize surfaces. *Nanoscale* **2022,** *14* (30), 10801-10815.

61. Ma, C.; Cai, W.; Zhou, T.; Zhang, C.; Zhang, Q.; Niu, H.; Wang, W., Versatile polyamides with new triphenylamine monomer based on dinaphtho furan as core for electrochromic/electrofluorochromic device, TNP detection and memory storage. *Sol. Energ. Mat. Sol. C.* **2024,** *272*, 112884.

62. Xu, S. Y.; Shi, W.; Huang, J. R.; Yao, S.; Wang, C.; Lu, T. B.; Zhang, Z. M., Single‐cluster Functionalized TiO_2 Nanotube Array for Boosting Water Oxidation and CO_2 Photoreduction to CH_3OH. *Angew. Chem. Int. Ed.* **2024,** *63* (28), e202406223.

63. Li, B.; Chen, M.; Hu, Q.; Zhu, J.; Yang, X.; Li, Z.; Hu, C.; Li, Y.; Ni, P.; Ding, Y., Facilely tunable dodecahedral polyoxometalate framework loaded with mono- or bimetallic sites for efficient photocatalytic CO_2 reduction. *Appl. Catal. B-Environ.* **2024,** *346*, 123733.

64. Wang, X.; Yang, M.; Gómez-García, C. J.; Cao, X.; Jin, Z.; Ma, H.; Pang, H.; Yang，G., Phase-Regulated $FeSe_2$@(1T-2H)-$MoSe_2$ Derived from Anderson-Type Polyoxometalate as an Efficient Electrocatalyst for the Nitrogen Reduction Reaction. *ACS Sustainable Chem. Eng.* **2025**, *13*, 1708-1718.

65. Zhao, L.; Yan, J.; Huang, H.; Du, X.; Chen, H.; He, X.; Li, W.; Fang, W.; Wang, D.; Zeng, X.; Dong, J.; Liu, Y., Regulating Electronic Structure of Bimetallic NiFe‐THQ Conductive Metal‐Organic Frameworks to Boost Catalytic Activity for Oxygen Evolution Reaction. *Adv. Funct. Mater.* **2023,** *34* (9), 2310902.

66. Zhuang, L.; Ge, L.; Liu, H.; Jiang, Z.; Jia, Y.; Li, Z.; Yang, D.; Hocking, R. K.; Li, M.; Zhang, L.; Wang, X.; Yao, X.; Zhu, Z., A Surfactant-Free and Scalable General Strategy for Synthesizing Ultrathin Two-Dimensional Metal-Organic Framework Nanosheets for the Oxygen Evolution Reaction. *Angew. Chem. Int. Ed.* **2019,** *58* (38), 13565-13572.

67. Li, C. F.; Zhao, J. W.; Xie, L. J.; Wu, J. Q.; Ren, Q.; Wang, Y.; Li, G. R., Surface-Adsorbed Carboxylate Ligands on Layered Double Hydroxides/Metal-Organic Frameworks Promote the Electrocatalytic Oxygen Evolution Reaction. *Angew. Chem. Int. Ed.* **2021,** *60* (33), 18129-18137.

68. Li, C. F.; Xie, L. J.; Zhao, J. W.; Gu, L. F.; Tang, H. B.; Zheng, L.; Li, G. R., Interfacial Fe-O-Ni-O-Fe Bonding Regulates the Active Ni Sites of Ni-MOFs via Iron Doping and Decorating with FeOOH for Super-Efficient Oxygen Evolution. *Angew. Chem. Int. Ed.* **2022,** *61* (17), e202116934.

69. Shen, Q.; Gómez-García, C. J.; Sun, W.; Lai, X.; Pang, H.; Ma, H., Improving the photocatalytic H_2 evolution activity of Keggin polyoxometalates anchoring copper-azole complexes. *Green Chem.* **2021,** *23* (8), 3104-3114.

Table of Contents

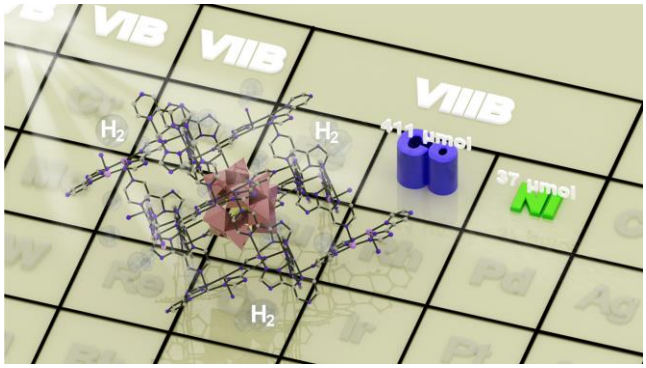

The construction of molecular junction through high-spin Co^{II} active sites promoted the generation of heteropoly blue states and enhanced the photocatalytic HER performance, and the photocatalytic HER activity of Co_6-GeW_{12} was as high as 13.7 mmol g^{-1} h^{-1}.